

**Design and Verification of the Hydraulic
Plantar Soft Tissue Reducer (HyPSTR):
Using Gated Magnetic Resonance Imaging to
Determine Mechanical Properties**

or

**Design and Verification of a Hydraulic
Device that Uses Gated Magnetic Resonance
Imaging to Determine Plantar Soft Tissue
Mechanical Properties**

Authors: please let us know which title you prefer

**Evan D. Williams,^{1,2} Michael J. Stebbins,^{1,2} Peter R. Cavanagh,^{2,3} David R. Haynor,⁴
Baocheng Chu,⁴ Michael J. Fassbind,¹ Vara Isvilanonda,^{1,2} William R. Ledoux,^{1,2,3}**

¹RR&D Center of Excellence for Limb Loss Prevention and Prosthetic Engineering,
VA Puget Sound, Seattle, WA, 98108;

²Department of Mechanical Engineering,

³Department of Orthopaedics & Sports Medicine,

⁴Department of Radiology

University of Washington, Seattle, WA, 98195

Corresponding author:

William R. Ledoux, PhD
ms 151, VA Puget Sound
1660 S. Columbian Way
Seattle, WA 98108
(206) 768-5347
(206) 764-2127 (f)
wrledoux@uw.edu

Keywords: heel pad; diabetes; MRI-compatible; mechanical properties

Abstract

Foot ulcers, perhaps caused in part by changes in the mechanical properties of the plantar soft tissue, can lead to lower limb amputations, especially in people with diabetes. The hydraulic plantar soft tissue reducer (HyPSTR) was designed as a tool to help understand, predict, and prevent ulcer formation by measuring *in vivo*, rate-dependent plantar soft tissue compressive force and three-dimensional deformations. These variables can be used in an inverse finite element analysis to determine tissue moduli, which are subsequently used in a foot model to show regions of high stress under a wide variety of loading conditions. The HyPSTR used an actuator to drive a magnetic resonance imaging (MRI) compatible hydraulic loading platform; pressure and actuator position were synchronized with MR image acquisition. Gated MRI will be used in future studies to record deformations at various phases during gait-like loading cycles applied by the platen. Achievable loading rates were slower than those found in normal walking because of a water-hammer (pressure wave ringing) effect in the hydraulics when the actuator direction was changed rapidly. The subsequent verification tests were performed at 0.2 Hz. The unloaded accuracy of the system was within 0.31%. Compliance, presumably in the system's plastic components, caused a displacement loss of 5.7 mm during a 20 mm actuator test. The positional accuracy of the HyPSTR during loaded displacement verification tests from 3 to 9 mm against a silicone backstop was 95.9% and the precision was 98.7%. The HyPSTR generated minimal artifact in the MRI scanner. Careful analysis of the synchronization of the HyPSTR and the MRI scanner was performed. With some limitations, the HyPSTR provided key functionality in measuring dynamic, patient-specific plantar soft tissue mechanical properties.

Introduction

Diabetes is a highly prevalent problem for healthcare in the United States with 9.3% of the population having the disease in 2014, leading to 60% of all non-traumatic amputations.¹ The disease has been shown to increase the modulus of plantar soft tissue in cadaveric samples,² which affects the ability of the foot to absorb and distribute energy from loading. As a result, peak stresses in plantar tissue near bony prominences can increase four fold or more³ and are thought to be the location of initial ulcer formation.^{3, 4} There is a need to improve current methods for predicting internal stress due to increases in plantar tissue stiffness. This can be accomplished by advancing the technology for measuring patient-specific soft tissue material properties. When combined with finite element analysis (FEA), we can better our understanding of foot mechanics and develop treatment options that are customized for individuals.

Ultrasound and fluoroscopic imaging have been used in plantar tissue analyses. Although these studies are the foundation for subsequent work, it is difficult to extrapolate volumetric information from them to generate three-dimensional (3D) patient-specific FEA models. Cavanagh⁵ mounted an ultrasound probe flush with an acrylic plate that measured skin-to-metatarsal head displacements upon foot contact. These measurements were one-dimensional (1D) and they collected load data in a subsequent test on separate equipment. Erdemir et al.⁶ utilized an ultrasound indenter in conjunction with dynamic loading and inverse FEA to develop hyperelastic material properties of the plantar fat pad. The device was capable of controlling the loading rate and recording patient-specific thickness, but the study approximates the fat pad as axi-symmetric and 1D with idealized boundary conditions. Gefen et al.⁷ used fluoroscopy and a force plate for simultaneous load and deformation collection but also found limitations in the single-dimensionality of the data and concerns with the fluoroscopy data collection protocol.

Progressing beyond ultrasound and fluoroscopy, magnetic resonance imaging (MRI), in conjunction with various non-metallic loading instruments, can also determine plantar tissue properties. Petre et al.⁸ developed a device that applied compressive loads to feet by holding hydraulic pressures for 3.5 minute static MRI scans. The resulting material properties could potentially be improved further by including strain rate dependent effects, which might be significant.² Gefen et al.⁹ employed a spherical indentation device to measure load vs. displacement of the plantar soft tissue between metatarsal heads. In addition to also being a static test, the <2N loads were much smaller than the subjects' weights and the skin, fat, and other subcutaneous tissues were lumped into one generic soft tissue. Another indenter study by Brown et al.¹⁰ addressed the viscoelastic dependency of tissue with an MRI-compatible piezoelectric device that accounted for strain and strain rate. The system has been used with tissue samples, but it is not understood if this technique can be applied to living subjects. Weaver et al.¹¹ performed dynamic MR elastography and determined that shear moduli differed with applied load. However, subjects voluntarily controlled the force and only two loading points were studied.

The purpose of this study was to develop a plantar soft tissue testing apparatus to that allows for dynamic loading, living subjects, normal walking force magnitudes and rates, hindfoot and forefoot positioning, patient-specific anatomy, and differentiation between soft tissue types. Hereafter, we report on the development and validation of the hydraulic plantar soft tissue reducer (HyPSTR), which loads the foot with a hydraulic system and records 3D tissue deformations with gated MRI.

Methods

System Design

The HyPSTR was designed to apply a cyclic, displacement-controlled load to either the forefoot or hindfoot while gated MRI obtained multiple phases (e.g., 16) of internal tissue deformation during loading and unloading. The force versus deformation data will be used as part of a subsequent study as inputs to an inverse FEA to solve for the patient-specific material properties of the plantar skin, adipose tissue, and muscle. A single-acting, master/slave hydraulic loading device produced triangle or sine shaped displacement curves of maximum amplitude of 10 mm at a theoretical loading rate up to 6 Hz and with a maximum load of 1500N. These parameters: 1) exceed the largest displacement necessary to approximate strain under body weight of the greatest plantar fat pad thickness expected;¹²⁻¹⁸ 2) incorporate the frequency content of gait¹⁹; and 3) allow for 1.1 x body weight forces for most people. (Note that while the maximum displacement and force were achieved, the 10Hz frequency, for reasons discussed in this paper, was not achieved.) Deformation of the soft tissue was determined by segmenting the MRI into specific tissue types.

All equipment in the MRI room was non-metallic, except for a few small, non-replaceable, but well secured, hardware items, while equipment in the control room, including all actuation, control, and data acquisition components did not have metallic restrictions (Figure 1). Electrical components were designed to minimize electromagnetic interference from the MR by utilizing twisted-pair shielded wiring, metal enclosures, and analog filtered signal lines. The displacement control system was built from a stepper motor-driven linear actuator (The Bug; Ultra Motion, Cutchogue, NY) and a stand-alone stepper driver (ST5-Si; Applied Motion Products Inc., Watsonville, CA).

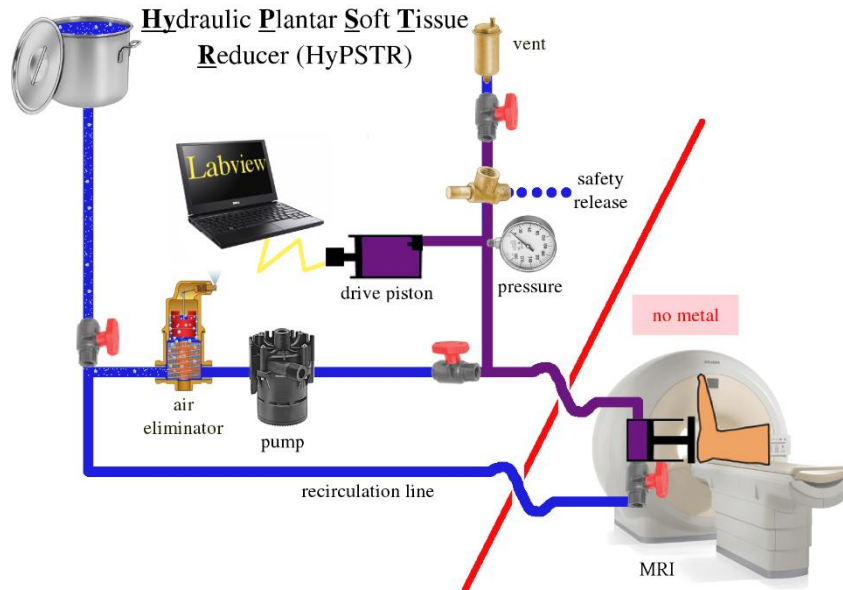


Figure 1. Instrument schematic showing fill and recirculation lines in blue and high pressure hydraulic lines in purple. Valves were closed to isolate the purple lines prior to testing.

A custom-designed, single acting, aluminum master piston/cylinder was attached to the actuator. The slave piston/cylinder was a similarly designed, single acting hydraulic system with equal bore diameter, but made of non-ferrous acetal plastic. A polycarbonate loading platen, threaded onto the end of the slave piston shaft, applied load to the plantar surface of the foot. The master and slave cylinders were connected via 9 m of 9.65 mm internal diameter, vacuum-rated nylon tubing that could withstand more than the 20 kPa negative pressure during the hydraulic retraction stage. Water was chosen as the hydraulic fluid because of its relative safety, availability, and ease of handling compared to various oils and gels. Once filled, a recirculating pump moved the water through a hydronic air eliminator (VJR075TM; Spirotherm, Glendale Heights, IL) to lower the dissolved gas under 50% to prevent entrained air bubbles from forming during system operation.

The stepper driver was controlled via the manufacturer-provided software, Q-Programmer. Custom LabVIEW software acquired and logged data, sent the displacement-synchronized trigger signal to the MR control center, and monitored the solenoid hydraulic safety valve. The software ran on a laptop computer (Intel Pentium M, 1.6 GHz, 2.0 GB RAM), which hosted an external data acquisition board (USB-6212, 400 kS/s, 16-bits; National Instruments, Austin, TX). All signals were acquired at 2500 Hz to allow for digital post-processing. The position and velocity of the linear actuator was determined from a rotary encoder affixed to the stepper motor (The Bug; Ultra Motion, Cutchogue, NY). The load applied to the foot was measured with a pressure transducer (PX209-200; Omega Engineering, Stamford, CT) installed in the hydraulic system. System pressure measurements during each of the sixteen phases were translated to applied force values with a calibration curve that was generated by using the HyPSTR to compress a piece of silicon in series with a 500 N load cell (MC3A-500; AMTI, Watertown, MA).

The test subject laid supine in an apparatus that supported the slave cylinder and loading platen and restrained the subject's foot, leg, and torso to minimize movement in the imaged volume that was not due to foot tissue compression (Figure 2). A hindfoot ankle-foot orthosis (American Artificial Limb, Seattle, WA) made from carbon fiber, leather, fiberglass, and Pe-Lite foam secured the lower leg while providing loading access to the heel via a cutout in the sole (Figure 3). This could be swapped for a second, forefoot ankle-foot orthosis that provided a backstop for the foot dorsum during forefoot testing. The slave cylinder could be adjusted in the anterior/posterior direction to align the loading platen with the center of the hindfoot or forefoot, and in the medial/lateral direction to adjust for left or right feet. To further minimize motion, the subject's torso was held in place with adjustable straps over the shoulders and around the waist

connected to a backboard that is integrated into the apparatus. All frame components and fasteners were polycarbonate, acetal plastic, nylon, fiberglass, polypropylene, or polyethylene (i.e., non-metallic).



Figure 2. Subject's leg and foot was secured by the (white) ankle-foot orthosis that is attached to polycarbonate rails. The slave cylinder (black) is in series with an ultrasound probe held in ABS plastic (yellow and red) and with a polycarbonate platen. Note the ultrasound probe was used to validate the system and it was removed before any MRI scanning was conducted.



Figure 3. Hindfoot (white) and forefoot (black) ankle-foot orthosis. The bolts on posterior surface are for mounting to the HyPSTR loading frame.

In an MRI, moving tissue can be imaged with cardiac gating, where short image phase acquisitions are triggered by the subject's heartbeat. Only objects with a periodic or quasi-periodic motion can be imaged in this manner,²⁰ which, in this study, referred to the loading platen frequency. Instead of using a heartbeat, phase synchronization was accomplished with a 2 ms peripheral pulse unit (PPU) signal sent from LabVIEW with a serial-to-fiber optic signal converter (Versalink; Electro Standards Laboratory, Cranston, RI). A pulse was sent upon the initial movement of the actuator from its zero-position and was then repeated at a user specified interval until test completion. The 3.0T Philips Achieva MRI Control and Data Acquisition System (Amsterdam, Netherlands) received this PPU and initiated the phase recording protocol in order to capture small portions of an image volume at specific times during a loading cycle (Figure 4). These partial acquisitions from each cycle were combined to generate complete images at each phase. Typically, 16 phases were generated.

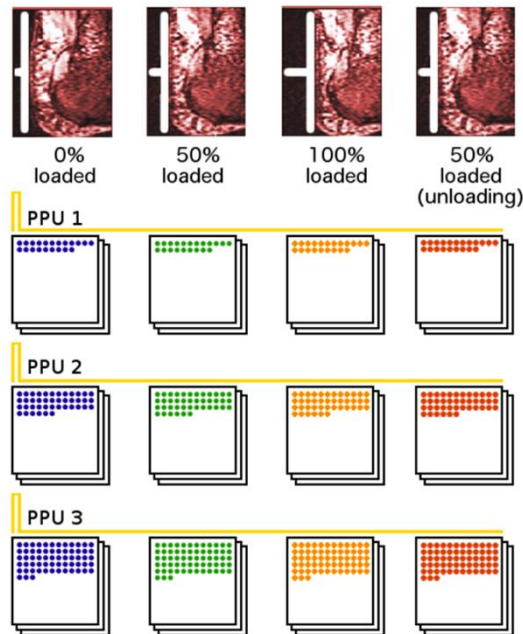


Figure 4. Gated MRI schematic showing 4 phase acquisitions for 3 cycles. The HyPSTR will collect approximately 16 phases over 250 cycles during subject trials.

The HyPSTR incorporated several redundant safety measures to protect the subject from over-loading and/or painful loading. An electronic, solenoid-operated hydraulic valve (Skinner 71295; Parker Hannifin, Cleveland, OH) was installed in the hydraulic system. When power is removed from the solenoid, the valve opens and the pressurized hydraulic fluid exits the system into a waste container, thereby removing load from the platen. Power to the solenoid could be removed by any of the following: an emergency-stop button near the test operator, an emergency-stop button at the test subject's side inside the MRI, by the system software if a patient-specific not-to-exceed pressure was surpassed, and by a virtual button on the LabVIEW front panel. The not-to-exceed pressure was the system pressure at the subject's ground reaction force increased by a factor of 1.2 to account for pressure surges. The emergency-stop button inside the MRI was fiber-optic and interfaced with a controller (both from Banner Engineering, Minneapolis, MN) inside the MRI control room. In case the solenoid failed, the hydraulic system also included an adjustable mechanical pressure relief valve. This valve was set to release any pressure greater than the patient-specific not-to-exceed pressure. As a final measure, the master piston was positioned in the master cylinder such that if it were to extend beyond a failed electronic limit switch, it could travel less than 1 mm before contacting the rigid aluminum cylinder bottom. The 1 mm buffer was a result of setting the location of the electronic limit switch by hand so as not to accidentally bottom-out the piston during cycling, which could damage the actuator.

Verification Testing

A series of verification tests were conducted to check the safety system and quantify the device's performance, operational capabilities, MRI compatibility, and PPU signal generation

timing. Data post-processing was performed in MATLAB (The Mathworks Inc., Natick, MA), Excel (Microsoft, Redmond, WA), and Image J (National Institute of Mental Health, Bethesda, MD).

The hydraulic plumbing integrity was tested by loading the system against a coil spring until the maximum design pressure of 1034 kPa was attained. The system was held at that level for a period of 10 minutes. Each element of the safety system was then tested with these conditions to ensure operation in the most critical situation.

The feasibility of simulating conditions similar to gait was assessed by implementing a 1 Hz triangle wave loading pattern. The repeatability of the HyPSTR was tested by conducting three separate fill/bleed/displacement test cycles of the hydraulic system at room temperature on three separate days. For each test, the empty hydraulic system was filled with fluid and air bubbles were bled. As a gold standard, a linear variable differential transformer (LVDT) was mounted in parallel with the platen. After bleeding, the system was cycled in a 0.2 Hz sinusoid ten times to 10 mm with no slave platen resistance to obtain baseline performance. We expected to observe 10 mm of platen movement for every 10 mm of driving actuator movement.

A pressure step test was performed by cycling the instrument through six stair-case profiles against a piece of silicone gel between the platen and a rigid backstop with the LVDT mounted in parallel with the platen. The silicone gel measured approximately 75 cm² with a thickness of 2 cm, and was chosen due to its viscoelastic similarity to biological soft tissue. For each cycle, the actuator was advanced in 2 mm increments from 0 to 20 mm with a three-second pause following each move. After pausing at 20 mm, the actuator returned to 0 mm in one continuous motion and then the next cycle commenced ($n = 6$). This entire process was repeated three times, approximately two hours apart, yielding a total of 18 stair-case data sets.

Sine wave displacement profiles with peak platen amplitudes of 3.0, 5.0, 7.0, and 9.0 mm (as determined by the LVDT mounted in parallel with the platen) were cycled for 30 minutes each. The same piece of silicone gel was placed between the loading platen and the load cell. A literature review found that unloaded adult plantar soft tissue under the metatarsals and calcaneus is generally between 5.4 and 26.5 mm thick, and that the maximum strain in the soft tissue beneath either location under body weight is approximately 0.45.¹²⁻¹⁸ For each test, the actual displacement of the loading platen vs. the prescribed displacement was analyzed at maximum extension for each cycle. The first 10 cycles' worth of data were excluded from that analysis due to preconditioning of the silicone gel. The root mean square error (RMSE) between a best-fit curve to the actual motor displacement and the prescribed displacement was calculated. Calibration curves correlating load on the platen to pressure in the system during loading and unloading were calculated for each displacement test.

The MRI-compatibility of the HyPSTR was determined by quantifying the influence of the loading device upon the obtained images.²¹ A fluid-filled MRI phantom was imaged under four separate conditions: the loading device not present on the MRI table, the device in place, the device in place with electrical power on, and the device in place with electrical power on and the platen moving. This was repeated with an MRI-compatible encoder attached to the platen. A central, 2D slice of the phantom was taken from each condition and the MRI-compatibility was calculated by computing the total pixel intensity delta between tests.

Gated MRI quality also depends on precise time synchronization. If the HyPSTR actuator motor is out of phase with the imaging protocol, then parts of the loading cycle will not be recorded and/or phases will seem out of focus, similar to motion blur. The three major sources of timing error come from: 1) delays or advances in the transmission of the PPU signal to the MRI

control hardware (i.e., the PPU offset), 2) discrepancy in the PPU generation period relative to the HyPSTR platen period (i.e., the PPU phase offset), and 3) other unknown sources. (There are also other minor offsets discussed in Appendix A.) The total error was determined by comparing the platen position as measured with the LVDT outside of the MRI core room to a subsequent scan with fiduciary markers adhered to the platen (Figure 5). Briefly, the HyPSTR was fully set up in the MRI scanning room with all tubing and fiber optic cables connected as in a normal scan. Then, taking advantage of the length of the cables, the HyPSTR was moved out onto the control room floor via the patient entrance of the MRI room; all the cabling remained connected and the LVDT was mounted in parallel to the platen. The unloaded platen was cycled 10 times, stopped and then repeated twice more (i.e., two more 10-cycle tests were conducted.) Once the test was completed and the LVDT was removed, the HyPSTR, which remained completely connected throughout, was returned to the MRI scanning room via the patient entrance, and two unloaded MRI tests were conducted while the fiduciary markers were imaged. Subsequently, the displacement of the platen in the MRI scanner was compared to displacement as measured by the LVDT. Since the volume of interest was considerably smaller than the foot, 29 phases, instead of 16, were collected. A least squares fit of the LVDT and platen data was conducted; the difference in timing of the peaks was the sum of all temporal errors.

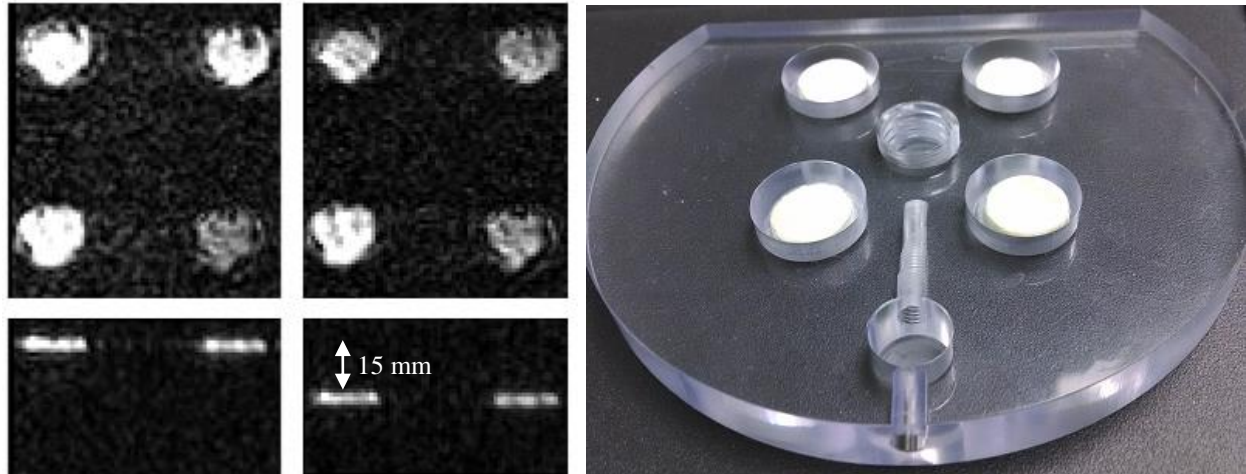


Figure 5. Platen markers from the starting position and the most extended position of a timing verification test. The platen is pictured on the right.

Results

A simple static pressure test with the coiled spring proved that the system did not have any major leaks, and high-pressure tests confirmed the proper functioning of all safety relief mechanisms.

The triangle-wave tests showed problems with the quality of the pressure signal at 1 Hz (Figure 6a); due to the rapid starting and stopping of the water column, a water hammer was observed. As such, 6 Hz speeds were never explored and instead, slowing the motor to 0.2 Hz and implementing a sine wave produced usable pressure data (Figure 6b). The 10 mm unloaded cycling tests were very accurate and repeatable, both within trials and between cycles, however there was some displacement loss, as the maximum slave platen movement was 9.68 ± 0.0076 mm, 9.65 ± 0.0082 mm, and 9.66 ± 0.0078 mm for the three separate trials. Further investigation showed that, due to machining inconsistencies, the master hydraulic piston diameter was approximately 96.5% as wide as the equivalent slave piston component. Hence the maximum displacement for the slave piston should be approximately 9.65 mm; all trials were

within 0.03mm or 0.31%. No bubbles were observed in the semi-translucent high-pressure tubing, indicating that the dissolved gas was being removed.

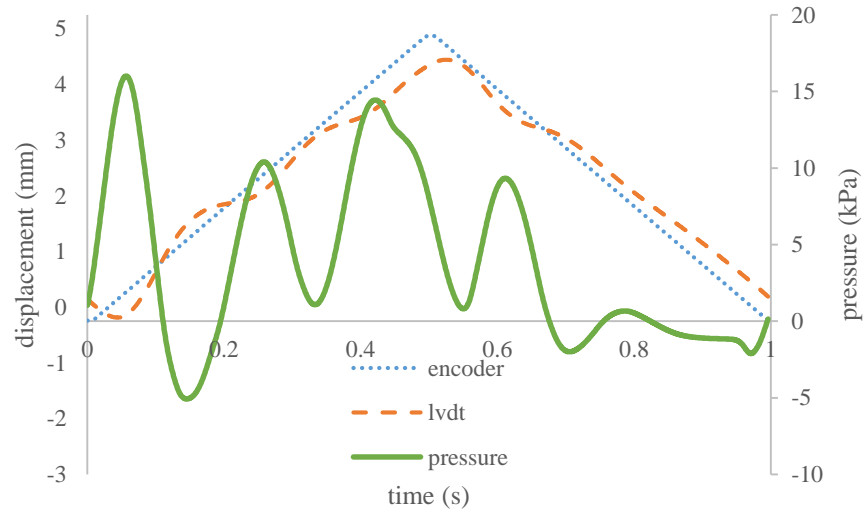


Figure 6a. Average of 240 triangle-wave cycles at 1 Hz and 5 mm actuator displacement. The ringing in the pressure signal (green) was indicative of a water-hammer. The sharp turnaround of the platen at each maximum and minimum position was too extreme for this hydraulic system.

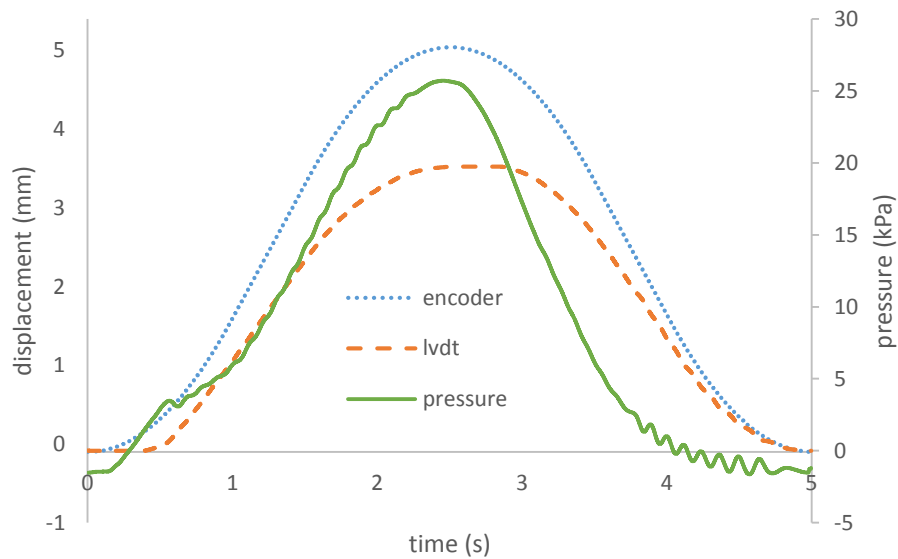


Figure 6b. Average of 240 sine-wave cycles at 0.2 Hz and 5 mm actuator displacement. The pressure signal ringing almost completely disappeared. The oscillations to the left of the maximum and minimum peaks were likely from the piston not being able to move smoothly past its friction point at slower velocities.

As load was incrementally increased against the silicone pads for the stepped pressure test, the encoder and LVDT measured a near-linear relationship between the master and slave displacements up to 8 mm (Figure 7a, b). Due to system compliance, non-linear losses occurred at the higher pressure values, where a 20 mm master displacement moved the slave platen only 14.3 mm. For each set of six stair-cases, the first stair-case was considered a pre-conditioning phase (i.e., the results were different from the other 5) and not included in displacement averaging, thus 15 stair-case profiles remained (Figure 7b).

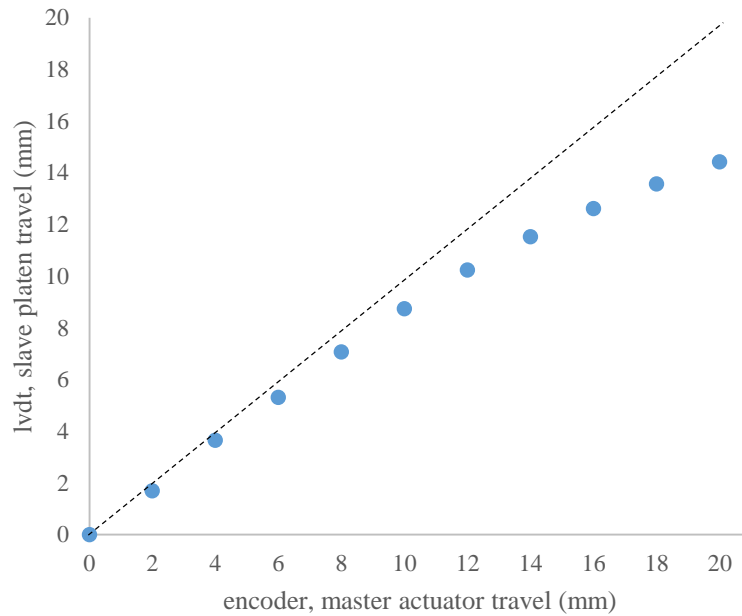


Figure 7a. Slave cylinder displacement vs. master cylinder displacement. Non-linear displacement loss occurred between the actuator and platen. Though the hydraulic components were chosen to be as rigid as possible, some system compliance still existed.

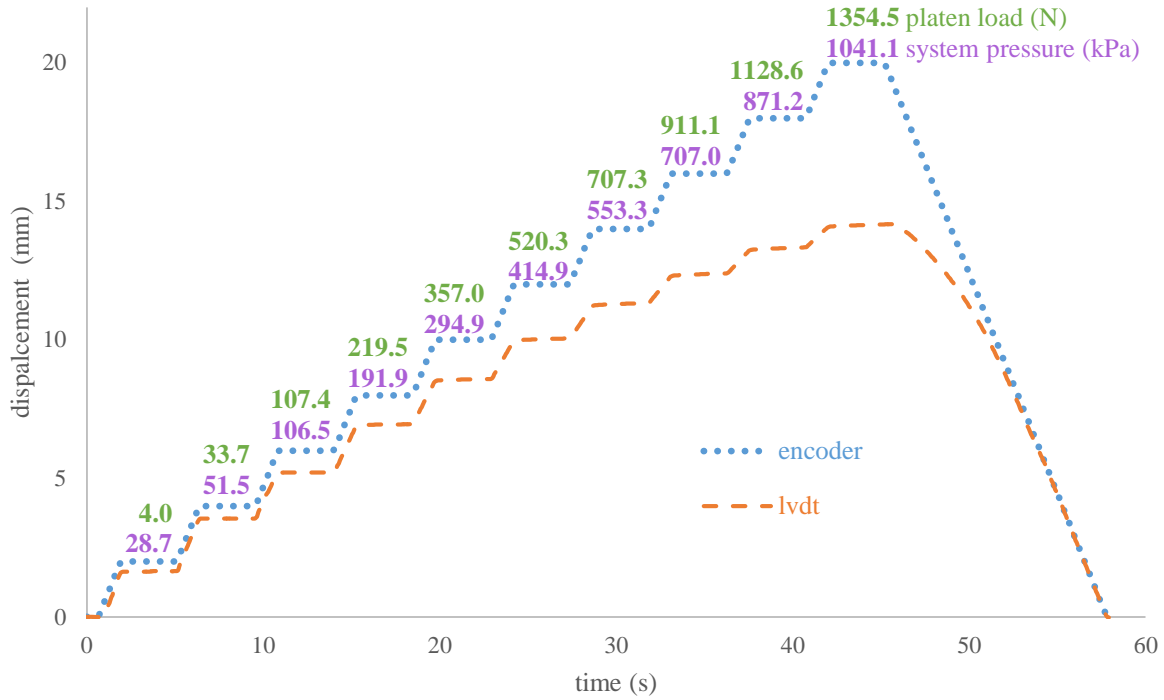


Figure 7b. Slave platen and. master cylinder displacement. The displacement loss was non-linear, becoming more significant with increasing master movement. It was approximated with a polynomial and used to calculate motor parameters for future tests.

The 30-minute loaded cycling tests for slave platen target positions had displacement and frequency accuracies near or below 1.0% in all but one condition. The displacements were least accurate in the 9 mm trial, while the frequencies deviated the most in the 3 mm trial (Table 1). Displacement precision (standard deviation divided by actual displacement) was 0.3% to 1.3% and frequency precision was 0.3% to 0.4% from mean values, depending on the target. (Note that these platen displacements generate the expected pressure range for subsequent *in vivo* testing.) A closer look at the average encoder movement and the target curve used to command the encoder demonstrated good tracking, with an RMSE of 0.002 mm (Figure 8). The LVDT displacement magnitude lagged behind the encoder because of the time required for the system to build up the approximately 30 kPa of pressure that was needed to overcome static friction in

the slave cylinder. Pressure-to-force calibration curves showed different patterns for loading vs. unloading (Figure 9). The effect of the static friction can be seen again on the bottommost and topmost parts of the loading curve, where changes in pressure did not immediately change the applied force.

Table 1. Accuracy and precision values for the HyPSTR under load from a piece of silicon. All data were from an LVDT attached to the slave platen.

Target displacement (mm)	Actual displacement (mm)	Error (%)	Target frequency (Hz)	Actual frequency (Hz)	Error (%)	Pressure (kPa)
3.000	3.05 ± 0.04	1.67	0.1775	0.1780 ± 0.0008	0.28	48.7
5.000	4.99 ± 0.06	0.20	0.1814	0.1816 ± 0.0006	0.11	104.1
7.000	7.074 ± 0.02	1.06	0.1794	0.1796 ± 0.0006	0.11	203.5
9.000	9.373 ± 0.08	4.14	0.1782	0.1785 ± 0.0005	0.17	351.8

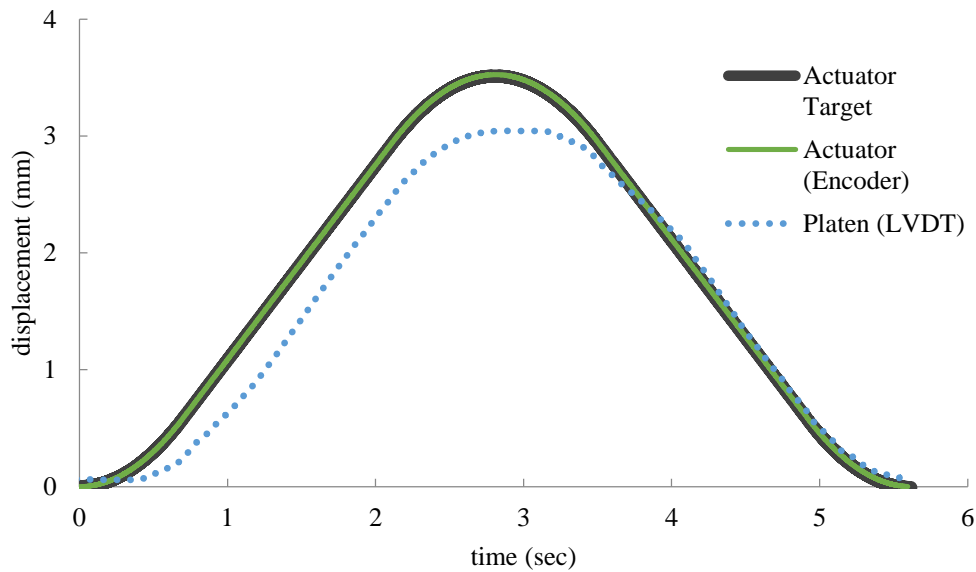


Figure 8. Overlap of the target sine wave used to set the motor control parameters and resulting encoder movement. The encoder path is nearly identical to the prescribed curve

(shown with an exaggerated thickness). The actuator/encoder had to move 3.526 mm to make the slave platen move 3.000 mm due to system compliance.

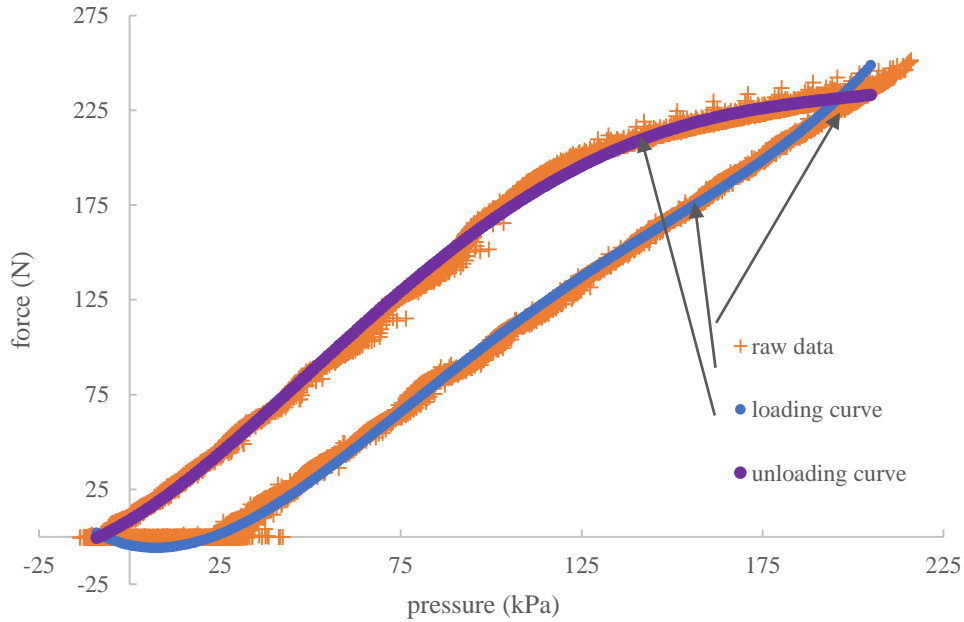


Figure 9. Pressure to force calibration curve from the 7-mm loaded verification test.

MRI imaging with a cylindrical phantom container in the acquisition volume showed no major artifacts (Figure 10a). The noncircular, grey shapes in the background were thought to be areas of water in the plumbing fittings and are located outside of the foot image volume. For comparison, a temporary addition of two 5 VDC copper wires to power an MRI-compatible encoder caused two parallel line defects to appear (Figure 10b). Numeric subtractions between summed image pixel intensities showed a difference of approximately 5% without the encoder, 7% with it (Table 2). The pixel quality observations did not indicate any significant artifacts, as confirmed by two radiologists.

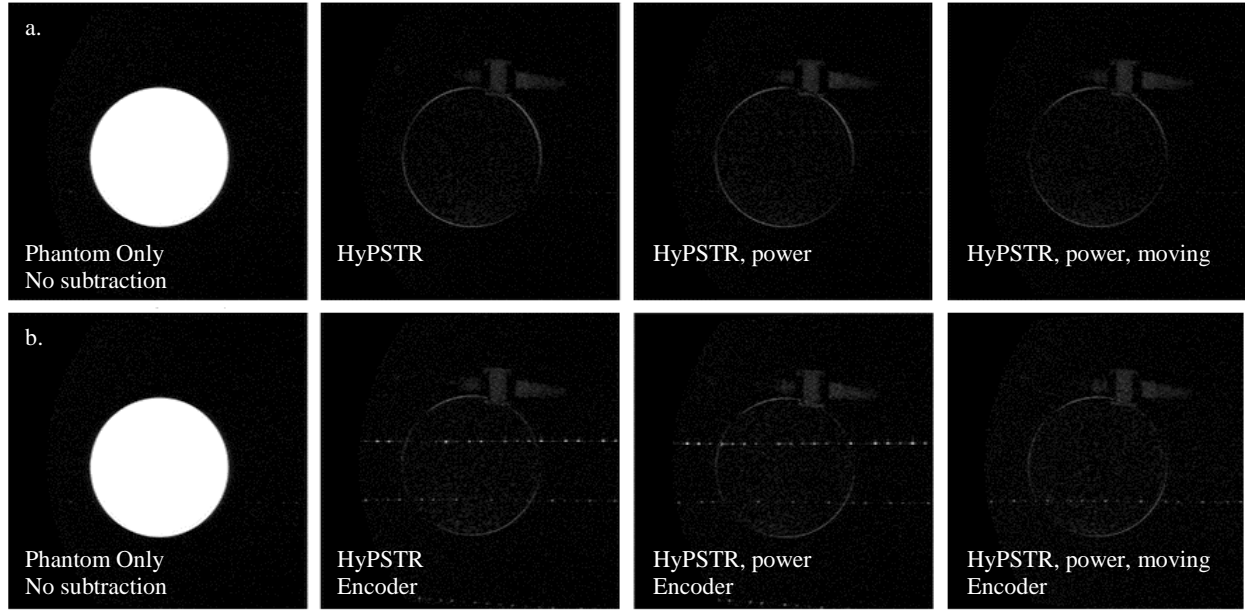


Figure 10. The leftmost images are of the control phantom without any hardware in the MR core. The darker images are subtractions from the same phantom, but different system configurations. Top row (a) is without the encoder, bottom row (b) is with the encoder. Second column is just hardware; third column is hardware plus power; fourth column is hardware, plus power, plus actuator motion.

Table 2. Quantitative artifact analysis. The tests with the MRI-compatible encoder increased artifact pixel intensity compared to those without the encoder.

Test Condition	Pixel Intensity (normalized)	Relative Intensity to Phantom Only (%)
Phantom only	1111615	100.0%
HyPSTR	58526	5.1%
HyPSTR, powered	60971	5.5%
HyPSTR, powered, moving	60320	5.4%
HyPSTR with encoder	73912	6.6%
HyPSTR with encoder , powered	76031	6.8%
HyPSTR with encoder , powered, moving	81300	7.3%

The two timing verification tests show that the platen position data from the MRI was collected 5.48 and 7.38 ms earlier than in the LVDT test. These values show a smaller than expected error; based on the measurable PPU offset and PPU phase offset, we expected the MRI data to be acquired approximately 39 ms early (Appendix A). This means that there is still a 31.5 to 33.5 ms advance offset that we are unable to locate. For a more in-depth explanation of the timing variables, please read Appendix A.

Discussion

Foot anatomy and material properties are unique to each individual and dependent on loading rates. If the tools used to assess foot mechanics (e.g., FEA models) are able to account for these subject specific differences, especially for populations with abnormally stiff plantar soft tissue such as persons with diabetes, this could lead to better treatment options. MRI is capable of providing the necessary image quality and tissue differentiation for these foot model improvements, but requires a compatible loading device. The functionality of the HyPSTR demonstrates that it is possible to build a non-metallic, hydraulic system with repeatable performance to 100% of a subject's dynamic ground reaction force while walking.

Our maximum cycle rate is currently 0.2 Hz because of the erratic pressure signals at higher frequencies. This is caused by a “water hammer”, which is a series of pressure reflections when attempting to rapidly reverse the momentum of the water column inside the hydraulic tubing. A pressure snubber could potentially be used to attenuate this ringing. Other possible solutions are to reduce the high-pressure tubing diameter to lower the mass of the water column or use a more compressible, viscous hydraulic fluid, such as glycol or oil, which can dampen the surges. The

tradeoff for all of these changes is lower platen force per unit of pressure, but it is still worth considering because the plantar fat pad modulus has been shown to change significantly between 1 Hz and 10 Hz loading in cadaver samples.²

The frequencies the vertical ground reaction of human gait would be more accurately simulated by impact loading profiles instead of sine waves. While virtually any motion profile may be programmed into the HyPSTR, it is currently limited to sinusoidal patterns that give cleaner pressure signals than a more appropriate (multi-frequency) triangle wave. Ultrasound instruments that permit true subject motion on a walking platform have a great advantage in this regard,⁵ but these devices generate two-dimensional data and are subject to trial-to-trial to variability.

The HyPSTR produces accurate and precise movement for both unloaded and loaded platen conditions. The hydraulics can apply enough force to equal the body weight of 138kg subject. Forces near this magnitude have been achieved before with MRI compatible devices,⁸ but not in conjunction with dynamic loading.

Pixel comparisons of a phantom object in the MR core during various configurations of equipment, power state, and movement show that there is little concern for artifact contamination in future foot data sets. An obvious problem was caused by a copper wire leading to a platen encoder; the encoder was removed to be certain that we recorded the highest image quality. Though it probably would have been acceptable to leave the encoder in place, there were additional issues with providing enough voltage to the sensor head over a 9 m long small gauge wire. A fiber optic potentiometer might have been a better choice,²² but commercial options were limited. Consequently, we were unable to generate an independent measure of displacement.

Instead, the four inset fiduciary markers provided a means of tracking the platen by generating a best fit plane parallel to the foot contact surface.

A detailed review of the timing errors from this study is presented in Appendix A. There were unknown errors of 31.5 to 33.5ms that have been empirically verified. Future tests would also account for the PPU offset, the PPU phase offset, other minor errors (i.e., pressure wave speed and zero detection), as well as an offset due to the number of HyPSTR cycles before imaging begins. Then, an additional factor of 32.5ms (averaged for the two trials here) should be included.

Although beyond the scope of this paper, this 32.5ms of unknown cause might be due to the serial to fiber optic PPU conversion that is required to read the PPU signal into the the MRI scanner. Additionally, once the PPU signal is received by the MRI scanner, there could be an internal delay with the system.

As discussed in Appendix A, the PPU offset was bimodal – either a large advance or a small delay/advance. The PPU initial generation is triggered when the LabVIEW VI detects movement of the rotary encoder that is attached to the actuator. The encoder is made up of alternating white and black patches whose widths define the measurement resolution. A change in detected color denotes movement, but if the encoder window is spanning two patches while at rest, the detection algorithm may think the hardware is moving immediately upon receiving power and before motion has begun. This would result in large delay. The small delay was believed to be random noise within the system resolution.

Future work will focus on exploring different hydraulic fluids, installing a double acting hydraulic piston, streamlining plumbing, and considering fiber optic encoders. These efforts will

lead to increased energy efficiency during displacement transfer, smoother/more responsive platen movement, lower probability of bubble entrapment, and better test-day control over loading variables. The data from this work will continue to be used as inputs and benchmarks for patient specific FEA foot models being developed in the same laboratory.²³ These models have the potential to improve the specificity of treatment approaches for both unique foot anatomy and complex deformities.

Diabetes prevalence is increasing in the United States; this disease causes both daily hardship and life-threatening complications. One manner of combating this disease is to preserve and increase any existing mobility in the patient population. In order to make an active lifestyle safe for people with diabetes, we need to prevent high stress regions, ulcer formation, and subsequent amputations. Approaching the problem on a case-by-case basis, with technology such as the HyPSTR, allows for the personalized treatment.

Acknowledgments

This work was supported by VA RR&D Grant A6973R. John Shaffer helped with design consultation and construction of the ankle-foot orthotics at American Artificial Limb, Seattle, WA.

References

1. National diabetes fact sheet, 2014. *Centers for Disease Control and Prevention* 2014.
2. Pai S, Ledoux WR. The compressive mechanical properties of diabetic and non-diabetic plantar soft tissue. *Journal of biomechanics*. 2010; 43: 1754-60.
3. Gefen A. Plantar soft tissue loading under the medial metatarsals in the standing diabetic foot. *Medical engineering & physics*. 2003; 25: 491-9.
4. Bakker K, Apelqvist J, Schaper NC, International Working Group on Diabetic Foot Editorial B. Practical guidelines on the management and prevention of the diabetic foot 2011. *Diabetes/metabolism research and reviews*. 2012; 28 Suppl 1: 225-31.
5. Cavanagh PR. Plantar soft tissue thickness during ground contact in walking. *Journal of biomechanics*. 1999; 32: 623-8.
6. Erdemir A, Viveiros ML, Ulbrecht JS, Cavanagh PR. An inverse finite-element model of heel-pad indentation. *Journal of biomechanics*. 2006; 39: 1279-86.
7. Gefen A, Megido-Ravid M, Itzchak Y. In vivo biomechanical behavior of the human heel pad during the stance phase of gait. *Journal of biomechanics*. 2001; 34: 1661-5.
8. Petre M, Erdemir A, Cavanagh PR. An MRI-compatible foot-loading device for assessment of internal tissue deformation. *Journal of biomechanics*. 2008; 41: 470-4.
9. Gefen A, Megido-Ravid M, Azariah M, Itzchak Y, Arcan M. Integration of plantar soft tissue stiffness measurements in routine MRI of the diabetic foot. *Clinical biomechanics*. 2001; 16: 921-5.
10. Brown PJ, Tan H, Stitzel JD. Displacement control device for dynamic tissue deformation in MRI - biomed 2010. *Biomedical sciences instrumentation*. 2010; 46: 99-104.
11. Weaver JB, Doyle M, Cheung Y, et al. Imaging the shear modulus of the heel fat pads. *Clinical biomechanics*. 2005; 20: 312-9.
12. Fields ML, Greenberg BH, Burkett LL. Roentgenographic measurement of skin and heel-pad thickness in the diagnosis of acromegaly. *The American journal of the medical sciences*. 1967; 254: 528-33.
13. Gooding GA, Stess RM, Graf PM, Moss KM, Louie KS, Grunfeld C. Sonography of the sole of the foot. Evidence for loss of foot pad thickness in diabetes and its relationship to ulceration of the foot. *Investigative radiology*. 1986; 21: 45-8.
14. Kanatli U, Yetkin H, Simsek A, Besli K, Ozturk A. The relationship of the heel pad compressibility and plantar pressure distribution. *Foot & ankle international*. 2001; 22: 662-5.
15. Kwan RL, Zheng YP, Cheing GL. The effect of aging on the biomechanical properties of plantar soft tissues. *Clinical biomechanics*. 2010; 25: 601-5.
16. Prichasuk S. The heel pad in plantar heel pain. *The Journal of bone and joint surgery British volume*. 1994; 76: 140-2.
17. Prichasuk S, Mulpruek P, Siri Wongpairat P. The heel-pad compressibility. *Clinical orthopaedics and related research*. 1994: 197-200.
18. Uzel M, Cetinus E, Ekerbicer HC, Karaoguz A. Heel pad thickness and athletic activity in healthy young adults: a sonographic study. *Journal of clinical ultrasound : JCU*. 2006; 34: 231-6.
19. Antonsson EK, Mann RW. The frequency content of gait. *Journal of biomechanics*. 1985; 18: 39-47.

20. Van de Walle R, Lemahieu I, Achten E. Magnetic resonance imaging and the reduction of motion artifacts: review of the principles. *Technology and health care : official journal of the European Society for Engineering and Medicine*. 1997; 5: 419-35.
21. Tsekos NV, Khanicheh A, Christoforou E, Mavroidis C. Magnetic resonance-compatible robotic and mechatronics systems for image-guided interventions and rehabilitation: a review study. *Annual review of biomedical engineering*. 2007; 9: 351-87.
22. Belforte G, Eula G. Design of an active-passive device for human ankle movement during functional magnetic resonance imaging analysis. *Proceedings of the Institution of Mechanical Engineers, Part H: Journal of Engineering in Medicine*. 2011; 226: 21-32.
23. Isvilanonda V, Dengler E, Iaquinto JM, Sangeorzan BJ, Ledoux WR. Finite element analysis of the foot: model validation and comparison between two common treatments of the clawed hallux deformity. *Clinical biomechanics*. 2012; 27: 837-44.

Appendix 1 – Timing Error Details

For reasons not completely understood, the PPU offset is bimodal; it was either early by several 100ms or it was within 20ms. This issue was solved by modifying the LabVIEW acquisition code to display the PPU signal and encoder position in real time. This allowed the operator to measure any initial delay or advance. If there was a significant PPU offset (i.e., greater than 20ms) in the initial PPU signal, then the HyPSTR was stopped and restarted. If the difference was less than 20ms, then data collection continued and it was accounted for later in post processing. For the verification trials in this study, the PPU error was approximately 2.5ms, once early and once late (Table A1).

The discrepancy between the PPU generation and HyPSTR platen periods (the PPU phase offset) was also determined. While the PPU generation was found to be very accurate and precise, i.e., always less than 0.5ms off of the scheduled transmission, the HyPSTR platen period was less accurate, e.g., 5012ms instead of 5000ms. This discrepancy could be minimized by choosing a PPU period to match the actuator movement (e.g., setting them both to 5012ms). For the verification trials, the PPU phase offset was less than 1ms (i.e., 0.821ms) per cycle; but the error accumulates over the course of the test (in this case, 78 cycles in 6.5min).

However, the fiduciary markers (and platen) were not exactly in the center of the image volume (Figure 5), and since the gated MRI acquisitions progressed from one side of the volume to the other, the amount of accumulated time error from the PPU phase offset was not simply the average over 78 cycles. Instead, the number of slices in the image volume were counted (in this case, 39) and divided by 78. This gave the fraction of a slice (in this case, 0.5) acquired by each pass of the gated MRI. The average PPU phase offset for the MRI scan was then found by taking

the average error accumulated by the first and last slices reached by the fiduciary markers and reported as the average PPU phase offset for region of interest (Table A1).

Two other relatively minor whole-test offsets (i.e., not per cycle) were realized. The speed of sound in water dictates the time for the pressure signal to travel through the hydraulic tubes to the slave platen. The platen motion was 4ms delayed from the master actuator motion. Relatively, the MRI acquisition was 4ms early (Table A1). There was also an offset of 7ms caused by our post processing code. At the trough of each sine wave cycle, the encoder output a series of “0.000000mm” values over a 14ms period. The displacement and pressure values from the processing code for each phase were reported by using the first “0mm” data point as the start time for each cycle. The true bottom of the trough was 7ms later. Relative to the processed displacements, the MRI acquisition was 7ms early (Table A1).

Finally, the first 10 phases of each test were ignored. The rationale was two-fold; it gave the operator time to check the PPU offset and allowed (in future loaded tests) for tissue preconditioning. This resulted in an 8.21ms delay (Table A1).

Table A1. MRI timing verification tests, showing expected phase acquisition offsets as calculated from measurable error. For a 6.5 min test at 0.2Hz there were 78 cycles.

Source of Timing Error	MRI marker Test #1	MRI marker Test #2
PPU offset (ms)	2.42 late	2.58 early
average PPU phase offset for region of interest (ms)	22.17 early	17.24 early
pressure wave speed (sound) (ms)	4 early	4 early
zero detection in post processing (ms)	7 early	7 early
PPU phase offset from 10 pre-image cycles (ms)	8.21 early	8.21 early

average error for the region of interest (ms)	38.96 early	39.03 early
error from timing verification	7.38 early	5.48 early
error of unknown cause	31.58 late	33.55 late
